Institute of Physics Publishing Measurement Science and Technology

Meas. Sci. Technol. **18** (2007) 275–287 doi:10.1088/0957-0233/18/1/034

An adaptive sampling and windowing interrogation method in PIV

R Theunissen[1], **F Scarano**[2] **and M L Riethmuller**[1]

[1] von Karman Institute for Fluid Dynamics, Chaussée de Waterloo 72, 1640 Sint-Genesius Rode, Belgium
[2] Department of Aerospace Engineering, Delft University of Technology, Delft, PO Box 5058, 2600 GB Delft, The Netherlands

E-mail: raf.theunissen@vki.ac.be

Received 21 August 2006, in final form 13 October 2006
Published 14 December 2006
Online at stacks.iop.org/MST/18/275

Abstract
This study proposes a cross-correlation based PIV image interrogation algorithm that adapts the number of interrogation windows and their size to the image properties and to the flow conditions. The proposed methodology releases the constraint of uniform sampling rate (Cartesian mesh) and spatial resolution (uniform window size) commonly adopted in PIV interrogation. Especially in non-optimal experimental conditions where the flow seeding is inhomogeneous, this leads either to loss of robustness (too few particles per window) or measurement precision (too large or coarsely spaced interrogation windows). Two criteria are investigated, namely adaptation to the local signal content in the image and adaptation to local flow conditions. The implementation of the adaptive criteria within a recursive interrogation method is described. The location and size of the interrogation windows are locally adapted to the image signal (i.e., seeding density). Also the local window spacing (commonly set by the overlap factor) is put in relation with the spatial variation of the velocity field. The viability of the method is illustrated over two experimental cases where the limitation of a uniform interrogation approach appears clearly: a shock-wave–boundary layer interaction and an aircraft vortex wake. The examples show that the spatial sampling rate can be adapted to the actual flow features and that the interrogation window size can be arranged so as to follow the spatial distribution of seeding particle images and flow velocity fluctuations. In comparison with the uniform interrogation technique, the spatial resolution is locally enhanced while in poorly seeded regions the level of robustness of the analysis (signal-to-noise ratio) is kept almost constant.

Keywords: PIV, image processing, adaptive interrogation, spatial resolution, aircraft wake vortex, shock-wave–boundary layer interaction

(Some figures in this article are in colour only in the electronic version)

Nomenclature

A	amplitude of flow fluctuation, expressed in pixels
b	transport aircraft model wingspan
C	cumulative density function
φ	two-dimensional sampling rate, expressed in samples per pixel^2 (spp)
h	grid spacing in the case of uniform sampling, expressed in pixels
λ_f	spatial wavelength of flow fluctuation, expressed in pixels
λ_w	spacing between neighbouring measurement points, expressed in pixels
M	cumulative density function
N_I	number of particles within the interrogation window

N_W	number of interrogation windows
OF	interrogation window overlap factor
p	probability density function
σ_u	velocity standard deviation
S_d	local seeding density, expressed in particles per pixel^2 (ppp)
SN	signal-to-noise ratio
u	horizontal velocity component
$\overline{u}$	mean velocity within interrogation window
v	vertical velocity component
X	downstream distance from aircraft wing
W_S	interrogation window size expressed in pixels
W_S^*	calculated interrogation window size based on seeding density

1. Introduction

Particle image velocimetry (PIV) has matured as a measurement technique enabling to describe the instantaneous planar velocity field from digitally recorded particle image motion. Nowadays the analysis of PIV recordings is most commonly performed via the two-dimensional spatial cross-correlation function over relatively small interrogation areas, obtained by image segmentation into so-called interrogation windows (Willert and Gharib 1991). The multi-grid analysis obtained by progressively refining the window size (Soria 1996) and deformation during iterative interrogation was demonstrated to increase both the accuracy and spatial resolution of the PIV technique (Fincham and Delerce 2000, Scarano and Riethmuller 2000). The deformation technique is important when dealing with flows with high velocity gradients.

Currently most interrogation parameters, namely the size of the interrogation window (W_S) and the overlap factor (OF) are set by the user and applied uniformly throughout the image, independent of variations in seeding density (defined as the number of particles per pixel) or flow property, even in the multi-grid analysis. Since the progressive window refinement is applied uniformly over the entire image, the interrogation process is unaware of the possible spatial non-homogeneity either in the side of seeding density or in terms of velocity fluctuations. Non-homogeneous information distribution occurs in the majority of the flows of interest. From this consideration a need arises to adopt more flexible interrogation algorithms. Previous studies have been dedicated to overcome this problem. At least two approaches can be identified: one is PTV and the second consists in making the correlation-based interrogation more flexible.

Particle tracking velocimetry (Hassan and Canaan 1991, Keane *et al* 1995) algorithms are based on the tracking of individual particle images and allow in principle the highest spatial resolution, i.e. one vector for each detected particle. However, pairing particle images in the presence of a large out-of-plane component still causes a lack of robustness. For this reason PTV algorithms were limited to flows with a low seeding density, with clear limits in spatial resolution. The super-resolution approach (Keane *et al* 1995, Stitou and Riethmuller 2001) incorporates conventional cross-correlation PIV followed by sub-grid particle tracking within the interrogation window. Despite the increased pairing success rate, tracking individual particles was shown to introduce larger noise due to the low precision of particle to particle matching (Spencer and Hollis 2005, Stanislas *et al* 2005). Because the cross-correlation PIV analysis provides an average displacement of an ensemble of tracers still representative of the in-plane motion, the advantage over PTV is the relative increase in robustness and precision.

For the analysis of PIV images by cross-correlation few attempts have been reported in the literature to adapt the cross-correlation analysis to the spatial variations in the seeding density (Rohály *et al* 2002, Susset *et al* 2006) or the cross-correlation signal as proposed by Wieneke and Susset (2004), who used the signal-to-noise ratio (SN ratio) as a criterion to increase the interrogation window. The SN ratio is defined as the ratio between the amplitude of the highest correlation peak versus the second highest. Rohly *et al* (2002) adapted the window size to the correlation signal within a reversed hierarchical structure. The proposed method starts with the smallest window size (2×2 pixels^2) and locally adds correlation maps (i.e., larger interrogation areas) until a reliable signal peak is found. Susset *et al* (2006) performed grid refinement and modified the window size depending on whether or not a valid result was obtained in the previous iteration. Both methods improved the spatial resolution through the ability to use larger windows in areas with low seeding density and to reduce the size in areas of high density. Indeed, application to experimental images showed promising performances. However, degradation of the correlation signal can also occur due to velocity gradients (none of the mentioned methods applies window deformation), therefore introducing ambiguous behaviour of the SN ratio with respect to the interrogation window size. The adjustment of the window size to the correlation signal can be seen as a signal adaptivity mechanism and to a small extent flow adaptation. Despite all improvements, the study of the cross-correlation map does not allow us to distinguish between a drop in the signal-to-noise ratio due to a lack in seeding particles or due to velocity gradients. On the other hand several procedures have been presented to incorporate adaptation to the spatial flow fluctuations. An algorithm to vary the interrogation window size with respect to the local velocity fluctuations has been proposed by Scarano (2002) for the analysis of vortex wakes. The shape of the windows can also be adapted to the local flow properties, namely flow direction (Di Florio *et al* 2002) or the velocity field curvature (Scarano 2003). The application of the above methods showed best results when applied within an iterative structure.

The present study follows the line of the latter method discussed and investigates separately the aspects of non-homogeneous seeding density and that of spatial velocity fluctuations, proposing a method that adapts the windows and sampling rate of the interrogation to varying seeding and flow properties by removing the unnecessary constraint of uniform windowing and placement of interrogation areas on a Cartesian mesh. The first part of the paper introduces the problem in general terms, discussing the concept of adaptive interrogation and its need under critical experimental conditions. The following section presents the implementation of the adaptive interrogation procedure followed by the application to experimental images from the wake vortex

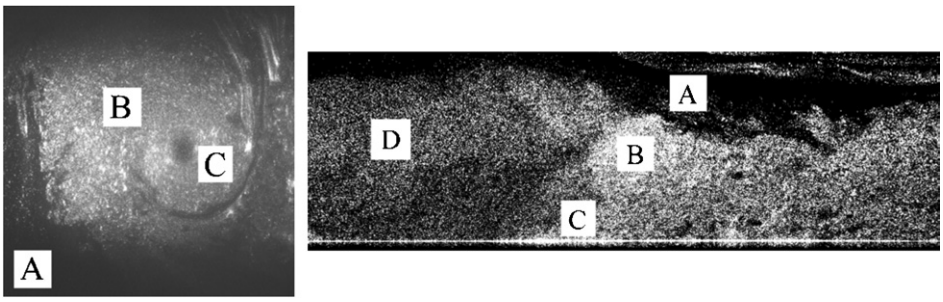

(*a*) (*b*)

Figure 1. PIV recordings of inhomogeneously seeded flows. (*a*) Aircraft vortex wake. (*b*) Shock-wave–boundary layer interaction.

behind a transport aircraft model and a supersonic flow over a shock-wave–boundary layer interaction.

2. Problem statement

When performing PIV measurements of complex flows, in some parts of the investigated domain a high spatial resolution might be required, i.e. small windows, whereas in other regions of the flow a lower spatial resolution may be sufficient. The conventional interrogation is optimized in a global sense and non-optimal conditions are often accepted in some regions of the measurement domain, which in turn introduces spurious vectors (when seeding density is too low) or large uncertainties due to poor spatial resolution. Two typical examples are shown where the user encounters a dilemma between the interrogation window size with respect to the seeding density, flow scales, non-homogeneous image and flow properties.

The first image shown in figure 1(*a*) is a recording with inhomogeneous seeding and illumination of a wake vortex behind a transport aircraft. As the external flow area 'A' is poorly illuminated, the particle image density is at such a level that no interrogation windows should be placed. Flow data can be extracted only in an area of about 80% of the image size, in which again a gradient in seeding density and flow scales can be found; region 'B' in the external flow has optimum illumination and seeding while a lower seeding level and smaller flow scales can be found in the vortex core ('C'). Figure 1(*b*) depicts an image of a shock-wave–boundary layer interaction, characterized by an intrinsically non-homogeneous seeding density due to compressibility effects (shocks) and temporal intermittency. Uniform flow regions (supersonic domains) are separated by sharp flow features (shocks, expansions). Empty regions as in 'A' would ideally require larger windows to collect enough particle images to yield a robust cross-correlation analysis. As no extra information on the flow itself can be obtained from 'A', only a few velocity vectors would suffice. Region 'D' is in the uniform flow upstream of the oblique shock, where small fluctuations in the velocity are to be expected. After the oblique shock impinges on the wind tunnel wall at 'C' where a turbulent boundary layer has fully developed (Humble *et al* 2005) a complex interaction exists in region 'B', characterized by sharp flow features in the form of the oblique shock and a thin shear layer emanating from the interaction point. In order to capture the large displacement difference associated with these features, a high spatial sampling rate is required. Preventing the shock from being smeared out would additionally necessitate the use of small interrogation windows to limit the well-known spatial filtering effect (Scarano 2002). Based on this line of thought the flow sampling rate should be varied throughout the recording with a higher sampling rate in 'B' and 'C' and a relatively lower one in 'A' and 'D'.

The resulting velocity field of the analysis with a constant interrogation window size distributed along a uniform mesh are presented in figures 2 and 3. When analysing the images with 64×64 windows and an overlap factor of 75% the number of outliers is limited (figures 2(*a*) and 3(*a*)). Nevertheless, because the seeding distribution is inhomogeneous, the poorly seeded flow in the peripheral regions of the vortex still introduces a large number of outliers. Due to the filtering effect the vortex core is most probably enlarged and will result in a smearing out of the expected vorticity peak. The shock wave and the flow close to the wall are sampled with relatively coarse spacing and with a window size probably larger than optimum. As such the spatial resolution is insufficient to adequately characterize the flow across the shock and the boundary layer properties.

Figures 2(*b*) and 3(*b*) present the results of the analysis performed with interrogation windows of 16×16 pixels^2 and an overlap of 75% ($h = 4$ pixels) yielding a spatial sampling rate of $1/h^2 = 0.0625$ samples per pixel^2. With the improved spatial resolution the shock locations in the case of the shock-wave–boundary layer interaction now become visible. The decrease in the final window size improved the spatial resolution, but also increased the number of outliers elsewhere in the recording since too few tracers were captured to perform a reliable correlation. Moreover, in the case of the vortex wake the flow spatial sampling rate is almost everywhere higher than necessary, since most of the high-frequency information is concentrated at the vortex core, which occupies less than 10% of the overall measurement area. These conflicting settings oblige the user to opt either for a high vector resolution in certain areas with a large number of outliers in other regions or for a low resolution with fewer outliers. Based upon a compromise between robustness/precision and resolution a window size of 32×32 is chosen in most cases.

3. Proposed methodology

The above examples demonstrate the need to suppress the unnecessary constraint of uniform spatial sampling (Cartesian grid) and constant interrogation window size over the whole

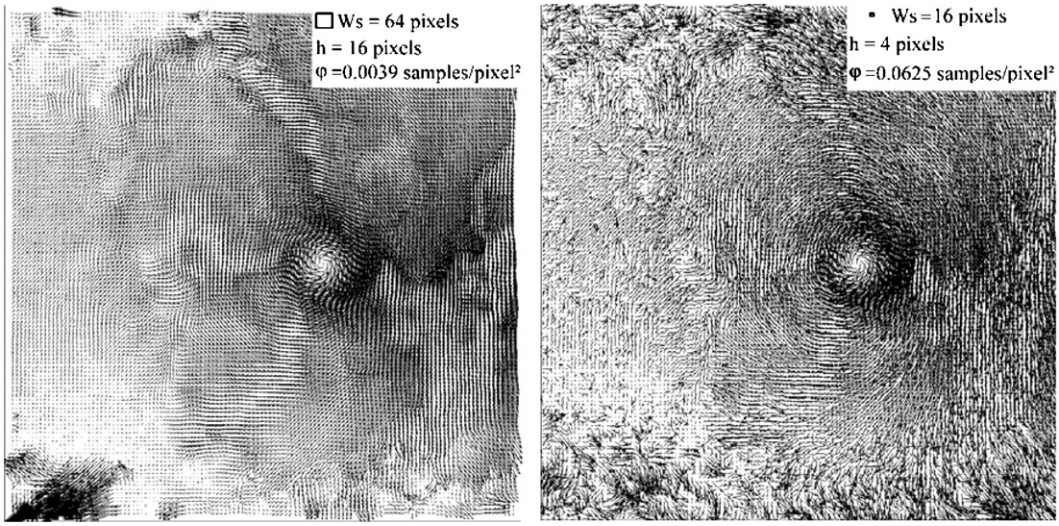

Figure 2. PIV analysis with uniform window size and uniform sampling rate (OF of 75%) of the recordings of the vortex wake. (*a*) W_S of 64 pixels, (*b*) W_S of 16 pixels (velocity field is undersampled by a factor of 4 in both directions for readability).

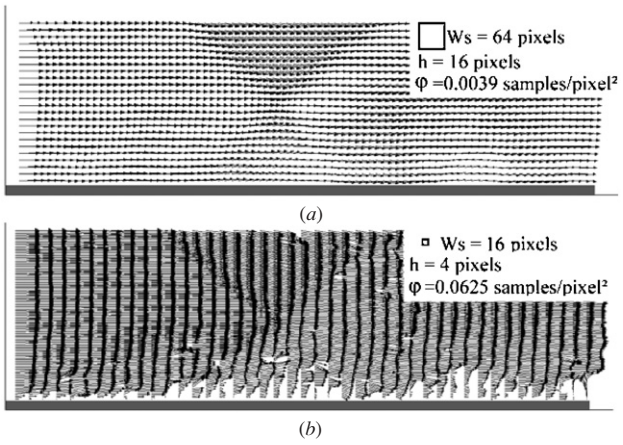

Figure 3. PIV analysis with uniform window size and uniform sampling rate (OF of 75%) of the recordings of the shock-wave–boundary layer interaction. (*a*) W_S of 64 pixels and (*b*) W_S of 16 pixels (velocity field is undersampled by a factor of 8 in the horizontal direction for readability).

domain of analysis. Instead, the measurement points should be chosen with a spatial density according to the local amount of available signal and flow scales.

Signal theory dictates that the smallest detectable wavelengths are determined by the Nyquist theorem, requiring a fluctuation to be sampled at least twice. From an experimental standpoint, this concept is of little use since one should know or estimate *a priori* how the velocity fluctuations are spatially distributed and what is their wavelength in order to apply the appropriate flow seeding. In experimental practice one tries to obtain the highest possible seeding density before multiple scattering or multiphase flow effects or excessive facility contamination occur.

The window size W_S is set by the user as a compromise between robustness and spatial resolution. The spatial sampling rate φ, defined as the number of samples per pixel^2 (spp), can then be varied through the window overlap OF. A uniform sampling with a grid spacing of h pixels corresponds to a two-dimensional spatial sampling frequency $\varphi = h^{-2} = [(1 - \mathrm{OF})W_S]^{-2}$. For the non-uniform sampling however the spacing, $\lambda_w(x, y)$, between neighbouring measurement points varies throughout the image and the spatial sampling rate may be defined as

$$\varphi(x, y) = \frac{1}{[\lambda_w(x, y)]^2}. \tag{1}$$

In the proposed methodology two main criteria are set for the adaptive windowing and sampling: signal adaptivity and flow adaptivity.

3.1. Signal adaptivity

In order to maintain an approximately constant number of particle images, N_I, within the interrogation window (Adrian 1991) W_S should be inversely proportional to the local seeding density S_d (in particles per pixel). The minimum amount of image pairs necessary to obtain a robust and accurate estimate of the displacement is somehow still under debate and may depend on the interrogation algorithm. However N_I ranges between 4 and 10 (Westerweel 1994, Raffel *et al* 1998). The available signal in the PIV recordings hence dictates the information that can be extracted from them, in turn determining the optimal size and location of the interrogation windows. The implementation of this criterion involves image pre-processing in order to estimate the amount of signal in the images (scattered light from the seeding particles).

A straightforward approach is to count individual particles over selected areas; well known in particle tracking velocimetry (Agüí and Jiménez 1987, Takehara and Etoh 1999). The particle detection algorithm is based on intensity background removal (sliding minimum subtraction, Wereley and Gui (2002)) and intensity thresholding (based on peak intensity histograms). For the required N_I the evaluation of S_d

returns the value of the window size based solely on the signal content $W_S{}^*$. The signal adaptivity criterion reads as

$$W_S^* = \frac{N_I}{S_d(x, y)} \tag{2}$$

while the spatial sampling rate φ is directly proportional to S_d (3):

$$\varphi \propto S_d. \tag{3}$$

An example of signal adaptation is shown in figures 4(*a*) and (*b*). A computer-generated PIV image has been produced with an inhomogeneous seeding density increasing from left to right (figure 4(*b*)). Following equations (2) and (3) more and smaller windows (represented by the red squares) are placed in those areas with a higher seeding density whereas the lower seeded regions are sampled more sparsely with enlarged interrogation windows.

3.2. Flow adaptivity

The flow fluctuations can be characterized by their amplitude A and spatial wavelength λ_f. Knowing their value would allow us to optimize the window size and to make an accurate estimate of the measurement error associated with the limited spatial resolution (Scarano 2003). In contrast to signal adaptation however both parameters are unknown *a priori* and the flow adaptivity criterion can only be implemented within a recursive structure. The presented methodology takes the estimator for the local spatial velocity fluctuations as the local velocity standard deviation over a kernel as large as the average interrogation window size.

After cross-correlation of the sampling windows a velocity field with pixel spacing is obtained through a linear interpolation of the individual vectors (see section 4). The calculation of the velocity standard deviation is then defined as

$$\sigma_u(x, y) = \sqrt{\frac{1}{W_S^2} \sum_{j=-\frac{W_S}{2}}^{j=+\frac{W_S}{2}} \sum_{i=-\frac{W_S}{2}}^{i=+\frac{W_S}{2}} [u(x+i, y+j) - \overline{u}]^2}. \tag{4}$$

In the above expression u is the horizontal velocity component varying throughout W_S, $\overline{u}$ and σ_u are the local mean and standard deviation within the kernel, respectively. The spatial sampling rate φ is also set directly proportional to σ_u (5):

$$\varphi \propto \sqrt{\sigma_u^2 + \sigma_v^2}. \tag{5}$$

The following example illustrates the above-described concept of flow adaptivity. Consider a jet-like Gaussian velocity distribution (figure 5(*b*)). The sampling rate is scaled according to the standard deviation and shows two peaks. The interrogation windows scaled by the standard deviation (according to equation (4)) are shown in figure 5(*a*), with a minimum size in the region of the largest velocity gradients.

3.3. Combination of signal and flow adaptivity

At the beginning of the iterative process, W_S is chosen large enough so as to obey the 1/4 rule (Adrian 1991). In the subsequent steps, the windows are gradually modified in size adapting locally to the seeding density distribution S_d and the velocity standard deviation σ_u. The algorithm used for the combined adaptation of the local window size reads as (6)

$$W_S = (1 + C_0 k) \cdot W_S^* \qquad \text{where} \quad k = \frac{\sigma_{\text{ref}} - \sigma_u}{\sigma_{\text{ref}}}$$
$$\text{and} \quad \sigma_{\text{ref}} = \text{median}(\sigma_u). \tag{6}$$

In the above equation W_S^* is the window size based on the evaluation of the local seeding density (2). The constant C_0 is set at 0.3 to limit the effect of flow adaptivity correction with respect to the signal adaptivity criterion (30% variation with respect to $W_S{}^*$). The range of k is limited between -1 and 1 in order to avoid too large fluctuations of k (and therefore W_S) in the case of spurious vectors.

Implementation of signal and flow adaptivity results in spatial distributions for both the velocity standard deviation and seeding density. The normalized product of σ_u and S_d is used to produce a spatial distribution for a single scalar, i.e. the spatial sampling rate φ (7). This is needed because the projection of the sampling positions is based on a single scalar distribution:

$$\varphi = \frac{S_d \cdot \sigma_u}{\iint_{\text{image}} S_d \cdot \sigma_u \, \mathrm{d}x \, \mathrm{d}y}. \tag{7}$$

During the first interrogation no information on the velocity distribution is available. Therefore the sampling rate will be based only on S_d. To distribute the sampling points in accordance with the value of the sampling rate φ use is made of the 2D transformation method (Secord *et al* 2002), which is summarized in the appendix. By updating the velocity field within an iterative structure, the local sampling rate and local window overlap factor will vary accordingly. The latter implies that the number of correlation windows may be freely adapted at every iteration. However, in the current implementation, the number of windows N_W is a constant and is determined solely by the number of identified particle images, imposed minimum number of tracers within the window N_I and mean area overlap OF (8). The latter is defined by the user prior to the interrogation process:

$$N_W = \frac{\text{Number of detected particles}}{N_I \cdot (1 - \text{OF})^2}. \tag{8}$$

The combination of σ_u and S_d represents the relative importance of the information contained over different areas in the image. As soon as the local velocity fluctuation increases, the displacement standard deviation will increase, requiring a higher sampling rate in that region (figure 6(*a*)). Concerning the signal distribution, the greater is the available signal, the closer smaller windows can be placed to each other, increasing the sampling rate and finally the spatial resolution. Eventually the PIV image with seeding density and velocity profile as depicted in figures 4(*b*) and 5(*b*) respectively is analysed with windows of non-uniform size located according to the calculated sampling rate (figure 6(*b*)).

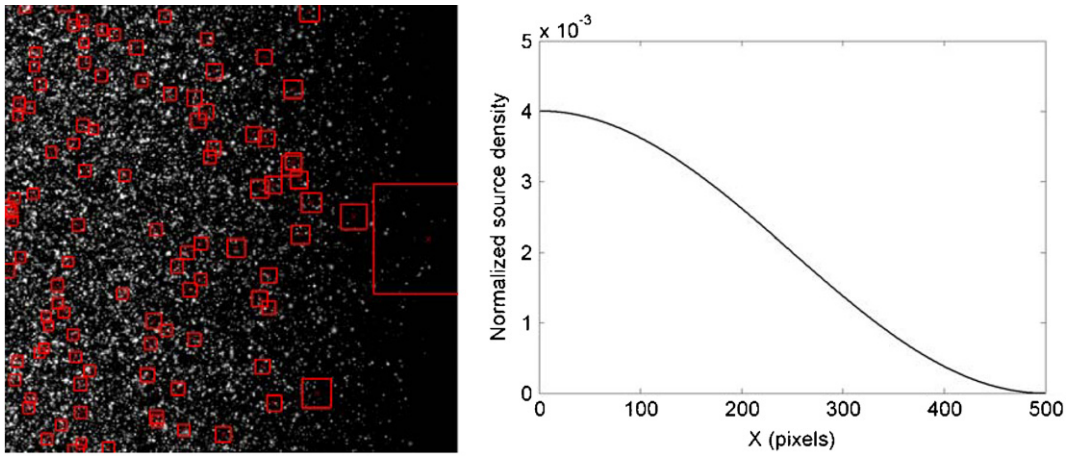

(*a*) (*b*)

Figure 4. (*a*) Generated PIV image with inhomogeneous seeding density and interrogation windows (red squares), (*b*) imposed, normalized seeding density.

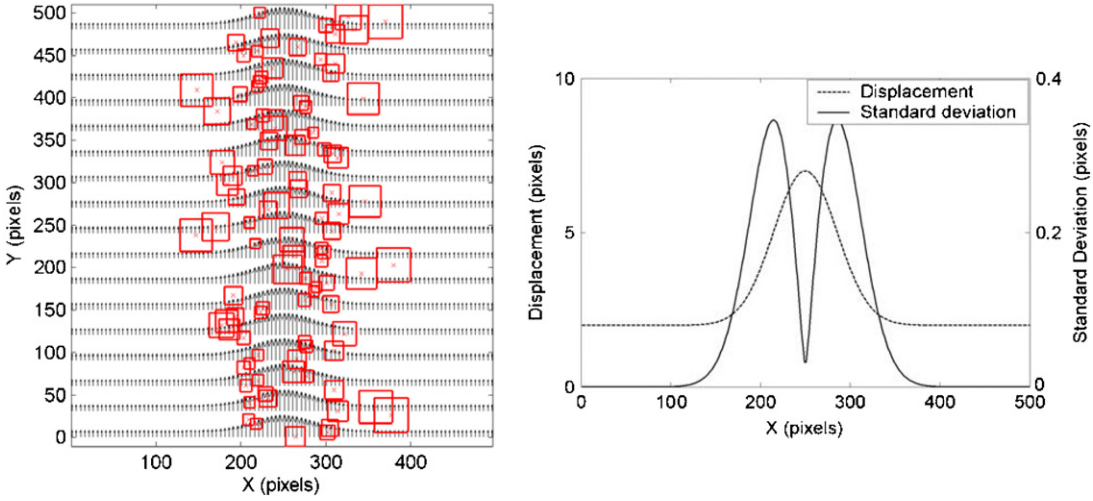

(*a*) (*b*)

Figure 5. (*a*) Imposed velocity field with interrogation windows (red squares), (*b*) imposed velocity profile and calculated standard deviation profile using moving windows of 27 pixels in width.

4. Interrogation method

Figure 7 schematically displays the outline of the implemented algorithm. The displacement is determined at the chosen locations by cross-correlating the interrogation windows with an iterative algorithm which applies window deformation following the WiDIM algorithm (Scarano and Riethmuller 2000). Four multi-grid steps are applied, followed by two iterative loops.

In the image deformation sequence, the displacements are linearly interpolated over all the pixels from an unstructured mesh of points using the nearest neighbours, i.e. locates for each pixel the three value points based on a Delaunay triangulation (Sambridge *et al* 1995). Prior to the interpolation, the predictor corrector iterative interrogation is stabilized with a least-squares fit (Scarano and Schrijer 2005). Each determined displacement vector is then reinterpolated using a second-order least-squares fit.

As the window size adaptation is driven by the velocity spatial fluctuations, the recently proposed normalized median test has been implemented as a validation procedure to eliminate spurious vectors (Westerweel and Scarano 2005). Erroneous vectors are then replaced by a linear interpolation of their direct neighbours.

In contrast to conventional interrogation processes, the proposed methodology returns displacement vectors placed on an unstructured grid. To allow further post-processing of velocity data the algorithm makes use of natural neighbour (NN) interpolation of the data to obtain a structured representation (Sambridge *et al* 1995). Though the NN interpolation allows a direct computation of the first-order derivatives, it was found that the final results were noisy. In order to retrieve smoother results for derivative operations, second-order polynomials were fitted onto the structured grid allowing a direct evaluation of, e.g., the vorticity.

The vortex image presented in figure 1(*a*) served as a test case to allow a comparison in the CPU time between

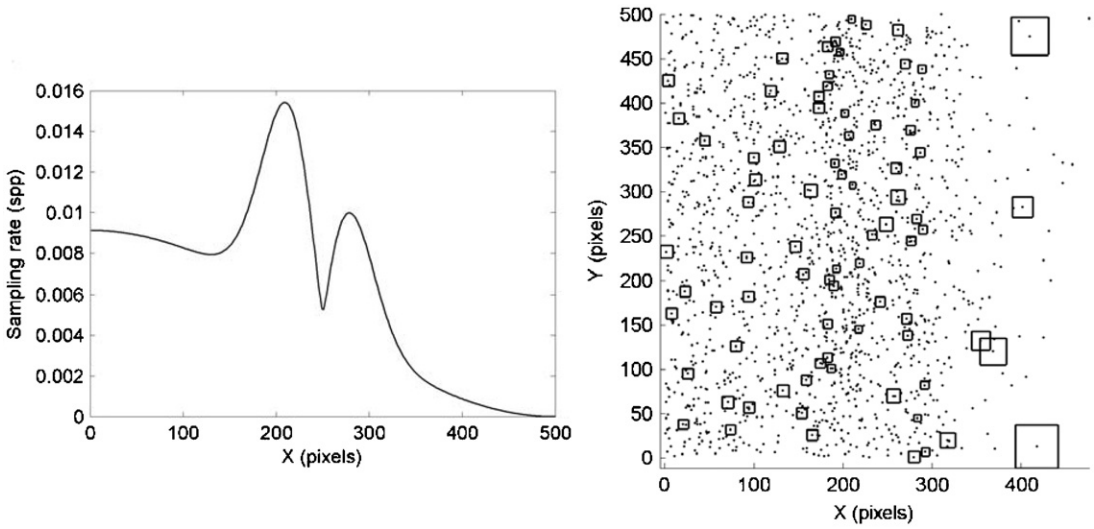

(*a*) (*b*)

Figure 6. (*a*) Sampling rate obtained as a linear combination between the velocity standard deviation and seeding density, (*b*) image of 16 000 interrogation windows distributed according to the sampling rate. The squares depict the size of randomly selected interrogation windows, calculated according to equation (6).

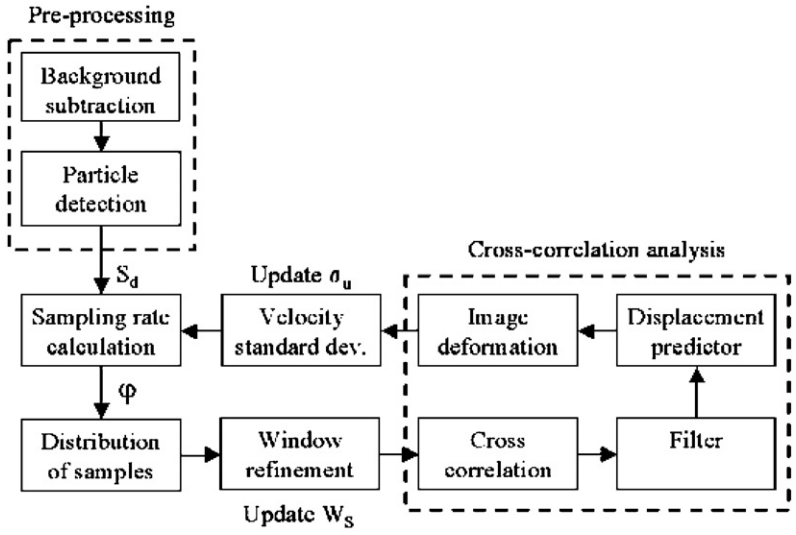

Figure 7. Block diagram of the implemented interrogation method.

WiDIM and the proposed adaptive methodology. Square windows of 41 × 41 pixels^2 with an overlap of 75% were imposed in the WiDIM process. The adaptive sampling and omission of superfluous correlation windows allowed the implemented technique to reduce the computation time by a factor of 2 compared to the classical approach. Figure 8 depicts the distribution in computation time over the different sub-processes for the two image processing methods. Distorting the images and cross-correlating the interrogation windows are in general the most computationally demanding. Figure 8(*b*) further indicates that the extra computational time associated with mapping and interpolation accompanying the sampling on an unstructured grid does not exceed 25% of the overall CPU time.

5. Performance evaluation

In this section the method is applied to two experimental cases: the wake vortex behind a transport aircraft and a shock-wave–boundary layer interaction (Humble *et al* 2005). The results from the current method are compared with those obtained with a conventional analysis from the improved WiDIM algorithm of DUTAE (Stanislas *et al* 2005).

5.1. Transport aircraft wake vortex

An aircraft model scale 1:48 is towed at 3 m s^{-1} in a water tank where 2C-PIV measurements are performed at a fixed station. The aircraft configuration at a few degrees incidence generates powerful vortical structures emanating

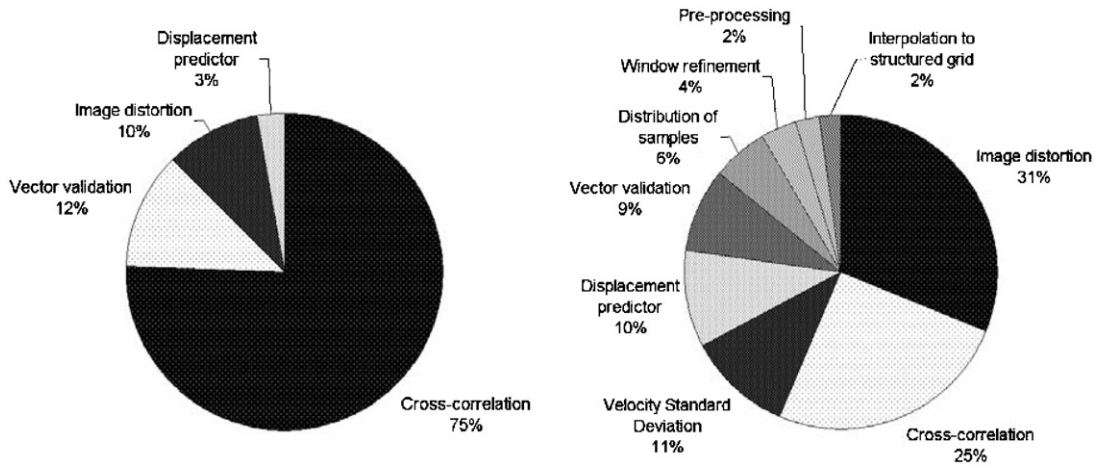

(*a*) (*b*)

Figure 8. Distribution in computational time: (*a*) WiDIM, (*b*) adaptive PIV.

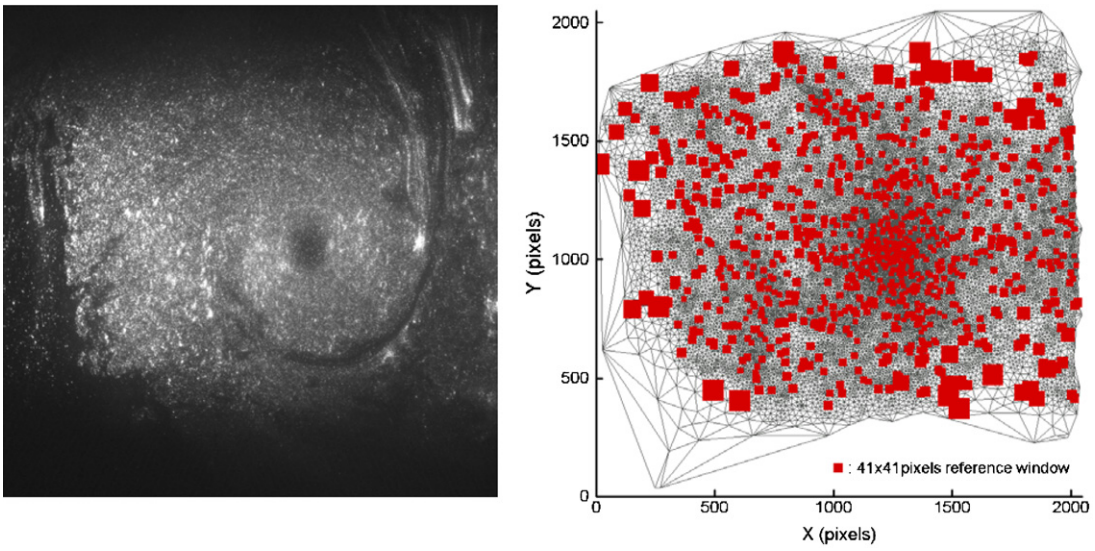

(*a*) (*b*)

Figure 9. Aircraft wake vortex: (*a*) instantaneous recording and (*b*) adaptive sampling (red squares represent selected interrogation areas, scaled with a factor of 2 for readability).

from wingtips, winglets and flaps. After a single vortex has formed, the circulatory motion persists with a considerable strength and lifespan downstream (Rossow 1999). Such a flow experiment has been selected because of some challenging and peculiar features. First, the imaged region covering a field view of 1.3×1.3 m^2 is neither uniformly seeded nor illuminated. Second, the flow properties are strongly non-uniform with small-scale fluctuations concentrated in a very small portion of the imaged flow, namely the vortex core. Figure 9(*a*) shows the recording of the wake vortex at $X/b = 30$, with the inherent large spatial variation in seeding where X is the distance downstream of the model and 'b' is the aircraft wingspan relating to a value of 1.25 m. By adapting the sampling rate to the seeding density and to the velocity standard deviation, samples are located in the region of interest, i.e. around the vortex core. Making use of the information on the velocity spatial fluctuations and that on the seeding density, a higher spatial resolution (higher sampling rate and smaller window size) can be obtained within the vortex core ensuring a better representation of its characteristics (figure 9(*b*)). As discussed in the introduction, processing the recorded images with a structured grid requires a trade-off for the choice of the interrogation area, between the number of outliers and spatial resolution. A constant sample area of 41×41 pixels^2 with an overlap of 75% was applied. The large number of outliers appearing strongly affects the representation of the vorticity field (figure 10(*a*) versus figure 10(*b*)). Moreover, because of the fixed distance between interrogation windows, the sampling of the vortex core is relatively poor ($h = 10$ pixels or $\varphi = 0.01$ spp), which results in an underestimation of the peak vorticity (-0.4 pixels/pixels) compared to the peak of -0.6 pixels/pixels obtained by adaptive PIV. The time history of vortex structure properties is important to determine the behaviour of the vortex in the mid field and far field. Figure 11 shows the time history of peak vorticity as obtained from WiDIM and from the adaptive method. Although the

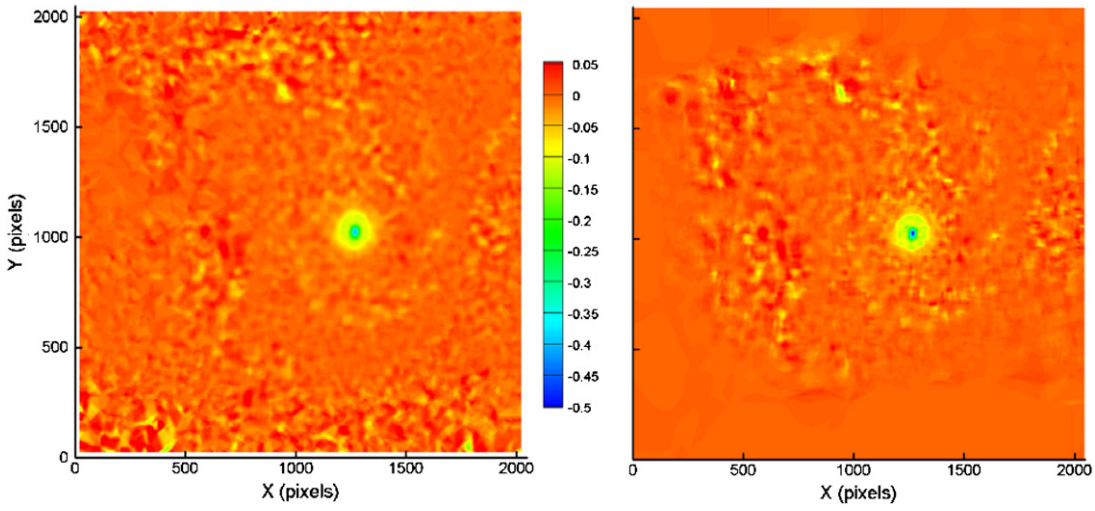

Figure 10. Vorticity field (pix/pix) of the wake vortex: (*a*) uniform sampling and (*b*) adaptive sampling.

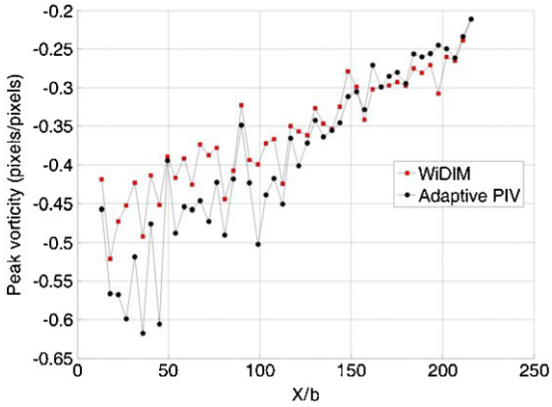

Figure 11. Time history of the peak vorticity: (■) WiDIM, (●) adaptive PIV.

diagram shows more scatter for the adaptive methodology, a constant underestimate can be observed for the data obtained from WiDIM. For $X/b > 100$ the discrepancy reduces as a result of the increase in the vortex core radius.

5.2. Shock-wave–boundary layer interaction

Experiments were performed in a Mach 2.1 free stream where the oblique shock wave generated by a wedge (deflection angle of 10°) impinges on the wind tunnel wall where a turbulent boundary layer has fully developed (Humble *et al* 2005). This case has been chosen because the flow seeding density experiences considerable spatial variations due to the flow compressibility (shown in figure 12). Moreover, seeding intermittency (figure 12) in the region of interaction makes the experimental conditions even more critical for a robust interrogation. From the flow features point of view, the challenging aspects are represented by the shock waves as well as the large range of flow scales associated with the turbulent boundary layer.

The analysis was performed over 400 image pairs. The images were processed with the adaptive scheme and WiDIM. In the latter case the interrogation was performed with 21×21 pix^2 and 75% overlap. For comparison at the end of the image interrogation process, the unstructured data were reinterpolated onto a grid of five pixels spacing.

Figure 12 shows the typical conditions encountered during the experiment. The seeding level close to the wall is relatively homogeneous due to vigorous turbulent mixing; however the external flow is affected by intermittency caused by the limited mass flow output of the seeding supply system. Turbulent structures also affect locally the seeding distribution with centrifugal forces that reduce the seeding level in the core of the vortices. The mean scattering pattern (figure 12(*d*)) clearly shows the variation in the seeding density associated with the flow density, which changes sharply across shock waves.

The contours of velocity magnitude clearly show the incident and reflected shocks as well as the boundary layer before and after the intersection (figure 13). From the spatial distribution of the mean interrogation window size, one can conclude that the adaptive algorithm automatically reduces the window size in the boundary layer and to some extent across the shocks. The uniform flow regions are therefore sampled with windows in the range of 37–45 pixels (figure 14). Across the λ-structure and after the interaction with the boundary layer, the variation in displacement is expected to increase. The window size is accordingly automatically scaled to a value ranging between 13 and 21 pixels. The flexibility in window sizing further allowed a gradual reduction of the calculated window size towards the interface with a maximum factor of 3/2. This reduction was simultaneously accompanied by an increase in the sampling rate. The instantaneous sampling distribution corresponding to the image presented in figure 4 is shown in figure 15. The adaptive sampling methodology places windows concentrated in those areas with sufficient tracers and in the area where the complex interactions take place.

The instantaneous displacement field corresponding to image (*b*) in figure 12 is depicted in figure 16. Contour levels are based on the calculated vorticity. Within the

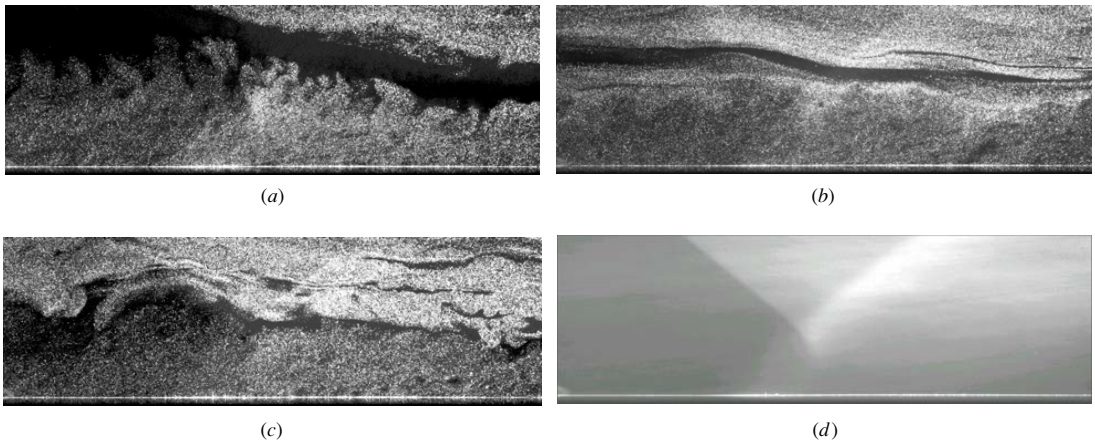

Figure 12. (*a*)–(*c*) Instantaneous PIV recordings of the shock–boundary layer interaction at different time instances. (*d*) Ensemble-averaged image intensity (400 image pairs).

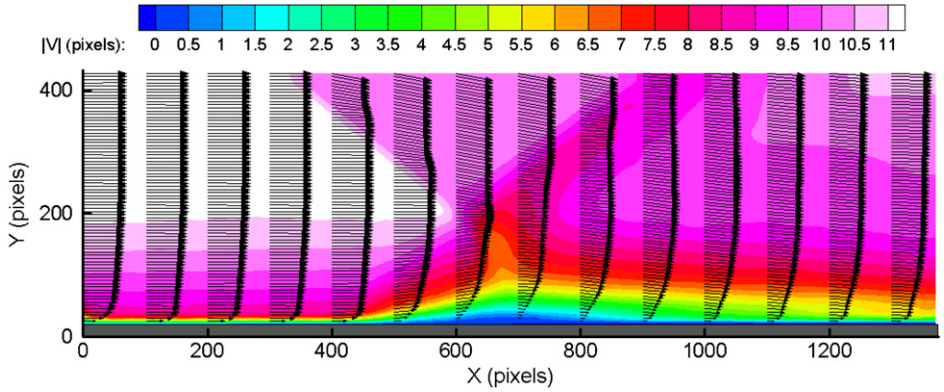

Figure 13. Ensemble-averaged velocity field with velocity profiles for the shock-wave–boundary layer interaction.

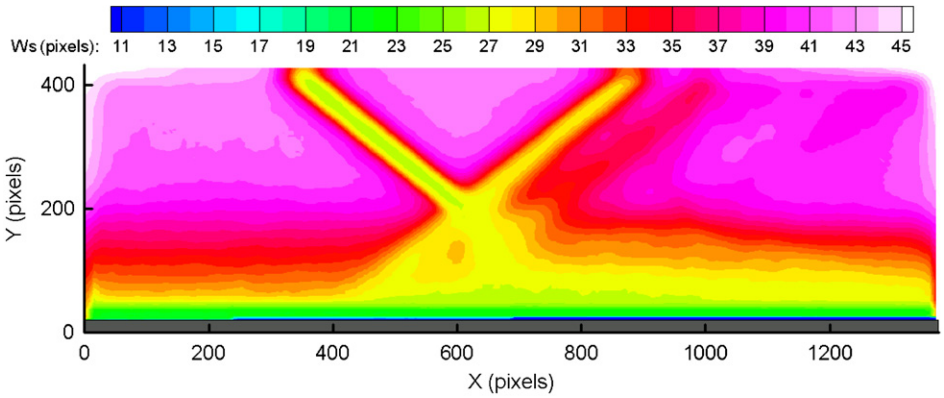

Figure 14. Ensemble-averaged window-size distribution for the shock-wave–boundary layer interaction.

free-stream regions, spurious peaks can be noticed when processing the image with WiDIM (figure 16(*a*)), indicating the presence of outliers. The adaptive methodology (figure 16(*b*)) on the other hand provides less noisy vorticity contours. Due to the augmented sampling rate near the wall, the adaptive methodology is furthermore able to return a smoother boundary layer velocity profile, especially upstream of the interaction region. Square windows of 21 pixels in size were used in the interrogation with WiDIM. According to the proposed window-size distribution by the adaptive process (figure 14) this is the minimum size to be applied in the bulk of the flow. Overall, the differences between the two methodologies are therefore small.

Ensemble-averaged velocity profiles obtained with both the adaptive and conventional methodology reveal no large differences in the bulk of the flow nor in the shock–wall interaction region (figure 17(*a*)). However, close to the wall a slight improvement can be observed with the velocity profile

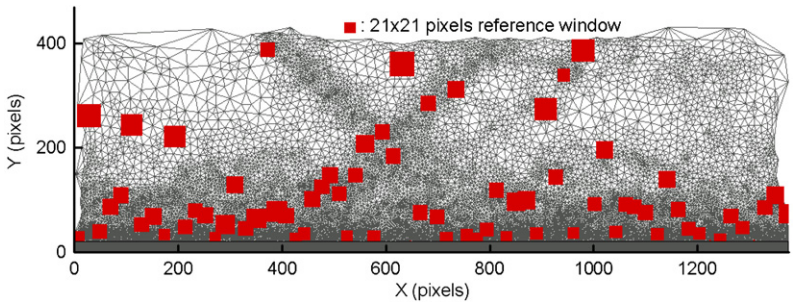

Figure 15. Unstructured mesh for a single snapshot of the instantaneous velocity field for the shock-wave–boundary layer interaction. Red squares represent selected interrogation areas.

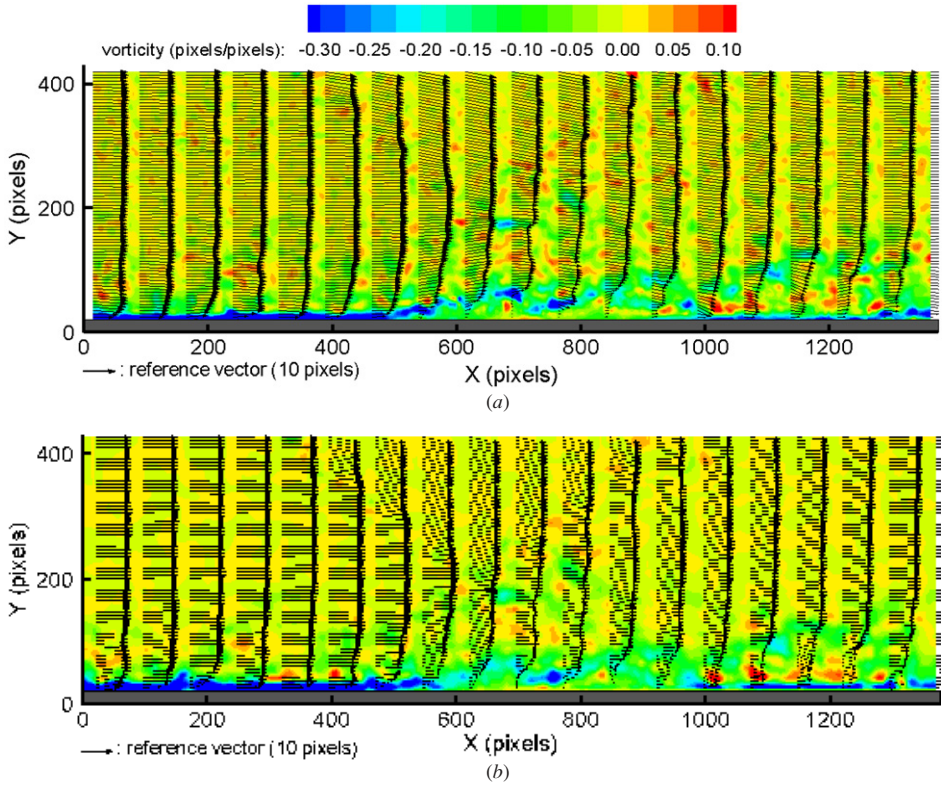

Figure 16. Shock-wave–boundary layer interaction instantaneous displacement field corresponding to image (*b*) in figure 12, with (*a*) uniform sampling and (*b*) adaptive sampling.

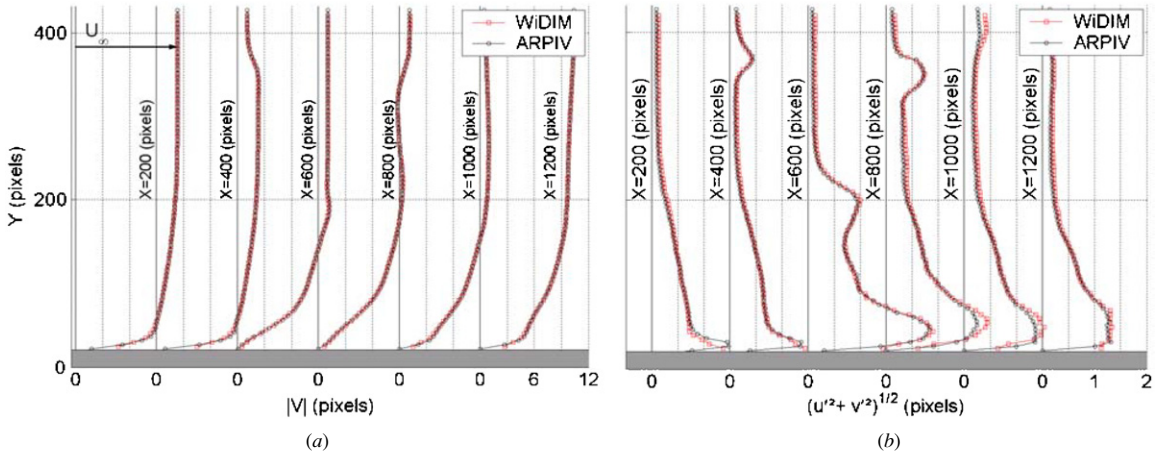

Figure 17. Extracted profiles of the ensemble-averaged (*a*) total displacement and (*b*) RMS in the displacement for the shock-wave–boundary layer interaction. (□) WiDIM, (○) adaptive PIV.

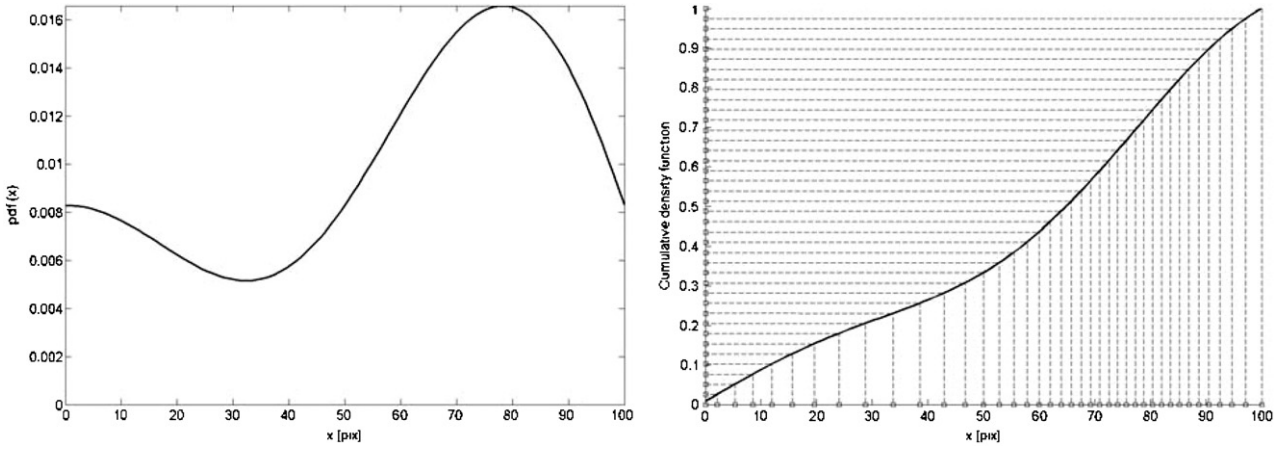

(*a*) (*b*)

Figure A1. (*a*) 1D probability density function and (*b*) its cumulative density function and regular sampling of its inverse.

approaching zero more systematically for the adaptive method. The extracted profiles of velocity fluctuations (figure 17(*b*)) show again that the adaptive and conventional analyses are quite comparable for this flow case, except for the trends approaching the wall where the adaptive method captures the peak better. Moreover, downstream of the interaction a slightly lower level of fluctuations is observed, which is ascribed to a lower occurrence of outliers.

6. Conclusions

An adaptive image interrogation method is proposed with the purpose of increasing robustness and spatial resolution. The location, number and size of the interrogation windows are related to the local number of particle images (i.e., seeding) and magnitude of the velocity fluctuations. The general criteria for flow adaptivity are stated treating separately signal adaptivity and flow adaptivity. The implementation of the adaptive methodology requires that interrogation windows are placed on an unstructured grid, which requires a technique for projection according to a target probability density function. The combination of the two criteria results in a single parameter describing the distribution of measurement windows.

Two experimental test cases have been chosen: an aircraft vortex-wake and a shock-wave–boundary layer interaction. In the first case the method automatically allowed the reduction of the number of outliers in poorly illuminated regions, still keeping a high resolution in the vortex core. In the second case the comparison with respect to a non-adaptive method yielded less-pronounced differences, due to smaller variations of the image properties, except in the case of seeding intermittency, which might occur in high speed flows.

Even when the performance of the adaptive technique did not yield a net improvement in the measurement, the fact that limited user input was needed (tuning window size and overlap factor) can be regarded as a significant improvement. Further efforts will be directed towards refined implementation of the criteria, such as boundary treatment and additional indicators for window refinement.

Acknowledgments

The PIV images of the shock-wave–boundary layer interaction were kindly provided by Ray Humble from TU Delft Aerospace Engineering. Geza Schrauf and Caren Huenecke from AIRBUS Bremen are acknowledged for the vortex wake images. This work is supported by the Instituut voor de aanmoediging van innovatie door Wetenschap & Technologie, Vlaanderen (IWT, contract no. SBO 040092) and by the Dutch Technology Foundation, STW (VIDI grant DLR.6198).

Appendix: pdf-weighted 2D point distribution

Let us consider a number of points to be distributed in space with the probability density function p as depicted in figure A1(*a*). The calculation of the cumulative probability function C (A.1) allows us to project randomly distributed points onto the target space (A.2), approximating the required sampling distribution (figure A1(*b*)). For illustration, regular separated points were chosen in figure A1:

$$C(x) = \int_0^x p(\eta)\,\mathrm{d}\eta \tag{A.1}$$

$$x_i = C^{-1}(p_i). \tag{A.2}$$

The procedure can be extended to two-dimensional signals. Given a 2D probability density function $p(x, y)$ defined on a domain of size $[L_x, L_y]$, then the marginal density function m and its cumulative density function M are given by the integrals in (A.3). Random values for the probability in x and y are chosen, $p_{x,i}$ and $p_{y,i}$. By taking the inverse of the cumulative density function M, the y-location of point i is retrieved (A.4):

$$M(y) = \int_0^y m(\eta)\,\mathrm{d}\eta \quad \text{where} \quad m(y) = \int_0^{L_x} p(x, y)\,\mathrm{d}x \tag{A.3}$$

$$y_i = M^{-1}(p_{y,i}). \tag{A.4}$$

Given y_i the x-coordinate x_i is determined by transforming $p_{x,i}$ according to the pdf at y_i, i.e. $p(x, y_i)$, by using the conditional

density function c and its cumulative C (A.5). The x-location is then given by the inverse of the latter function (A.6)

$$C(x|y_i) = \int_0^x c(\eta|y_i)\,\mathrm{d}\eta \quad \text{where} \quad c(x|y_i) = \frac{p(x, y_i)}{m(y_i)} \tag{A.5}$$

$$x_i = C^{-1}(p_{x,i}|y_i). \tag{A.6}$$

References

Adrian R J 1991 Particle-imaging techniques for experimental fluid mechanics *Ann. Rev. Fluid Mech.* **23** 261–304

Agüí J C and Jiménez J 1987 On the performance of particle tracking *J. Fluid Mech.* **185** 447–68

Di Florio D, Felice F D and Romano G P 2002 Windowing, reshaping and re-orientation interrogation windows in particle image velocimetry for the investigation of shear flows *Meas. Sci. Technol.* **13** 953–62

Fincham A and Delerce G 2000 Advanced optimization of correlation imaging velocimetry algorithms *Exp. Fluids Suppl.* **29** S13–S22

Hassan Y A and Canaan R E 1991 Full-field bubbly flow velocity measurements using a multiframe particle tracking technique *Exp. Fluids* **12** 49–60

Humble R A, Scarano F, van Oudheusden B W and Tuinstra M 2005 Experimental study of an impinging shock wave/turbulent boundary interaction using PIV *36th AIAA Fluid Dynamics Conf. and Exhibit* paper AIAA-2006-3361

Keane R D, Adrian R J and Zhang Y 1995 Super-resolution particle imaging velocimetry *Meas. Sci. Technol.* **6** 754–68

Raffel M, Willert C F and Kompenhans J 1998 *Particle Image Velocimetry—A Practical Guide* (Berlin: Springer)

Rohály J, Frigerio F and Hart D P 2002 Reverse hierarchical PIV processing *Meas. Sci. Technol.* **13** 984–96

Rossow V J 1999 Lift-generated vortex wakes of subsonic transport aircraft *Prog. Aerosp. Sci.* **35** 507–660

Sambridge M, Braun J and McQueen H 1995 Geophysical parametrization and interpolation of irregular data using natural neighbours *Geophys. J. Int.* **122** 837–57

Scarano F 2002 Review article: iterative deformation methods in PIV *Meas. Sci. Technol.* **13** R1–R9

Scarano F 2003 Theory of non-isotropic spatial resolution in PIV *Exp. Fluids* **35** 268–77

Scarano F and Riethmuller M L 2000 Advances in iterative multigrid PIV image processing *Exp. Fluids Suppl.* **29** S51–S60

Scarano F and Schrijer F F J 2005 Effect of predictor filtering on the stability and spatial resolution of iterative PIV interrogation *6th Int. Symp. on PIV (Pasadena, USA)*

Secord A, Heidrich W and Streit L 2002 Fast primitive distribution for illustration *13th Eurographics Workshop on Rendering* ed P Debevec and S Gibson

Soria J 1996 An investigation of the near wake of a circular cylinder using a video-based digital cross-correlation particle image velocimetry technique *Exp. Therm. Fluid Sci.* **12** 221–33

Spencer A and Hollis D 2005 Correcting for sub-grid filtering effects in particle image velocimetry data *Meas. Sci. Technol.* **16** 2323–35

Stanislas M, Okamoto K and Kähler C 2005 Main results of the second international PIV challenge *Exp. Fluids* **39** 170–91

Stitou A and Riethmuller M L 2001 Extension of PIV to super-resolution using PTV *Meas. Sci. Technol.* **12** 1398–403

Susset A, Most J M and Honoré D 2006 A novel architecture for a super-resolution PIV algorithm developed for the improvement of the resolution of large velocity gradient measurements *Exp. Fluids* **40** 70–9

Takehara K and Etoh T 1999 A study on particle identification in PTV—particle mask correlation method *J. Vis.* **1** 313–23

Wereley S T and Gui L 2002 Advanced algorithms for microscale particle image velocimetry *AIAA J.* **40** 1047–55

Westerweel J 1994 Efficient detection of spurious vectors in particle image velocimetry data *Exp. Fluids* **16** 236–47

Westerweel J and Scarano F 2005 Universal outlier detection for PIV data *Exp. Fluids* **29** 1096–100

Wieneke B and Susset A 2004 Higher PIV accuracy by optimization of interrogation window size and shape *Pivnet T5/ERCOFTAC SIG 32, 7th Workshop on PIV (Lisbon, Portugal)*

Willert C E and Gharib M 1991 Digital particle image velocimetry *Exp. Fluids* **10** 181–93